



Exploration on flutter mechanism of a damaged transonic rotor blade using high-fidelity fluid–solid coupling method

Chunxiu Ji¹, Zijun Yi¹, Dan Xie^{1,†} and Earl H. Dowell²

¹School of Astronautics, Northwestern Polytechnical University, Youyi West Road 127#, Xi'an 710072, PR China

²Duke University, Durham, NC 27708-0300, USA

(Received 16 January 2024; revised 25 June 2024; accepted 14 September 2024)

Structural damage in turbomachinery is a primary origin of aeronautic accidents, which is receiving increased attention. This study is thus focused on the aeroelastic analysis of damaged blades, including the onset of flutter and underlying mechanisms. First, a high-fidelity fluid–solid coupling system is established with computational fluid dynamics (CFD) and computational structural dynamics (CSD) technologies, via which the dynamic aeroelastic analysis is conducted based on static aeroelastic deformation. Second, a damaged rotor blade is parametrically modelled with variable damage levels, extents, and positions. Finally, the modal identification method of spectral proper orthogonal decomposition (SPOD) is applied to observe flow details and provide physical insight into the flutter mechanism for damaged blades. Numerical analysis finds that there is a critical damage level below which the aeroelastic stability is positively improved with increasing damage level; otherwise, a significant loss of stability is induced. The damage location and extent further affect this critical damage level and the change rate crossing the threshold. The simulation with CFD/CSD finds that the high pressure near the trailing edge induced from boundary layer separation suppresses vibrations in stable conditions, but motivates vibrations during flutter, which is because of the high-pressure spread to nearing blades. SPOD modes reveal that high-frequency disturbances with large scale are primary factors inducing flutter, which is further stimulated by the high-order disturbances with small scale. This study provides a crucial foundation for the fatigue prediction for rotor blades in service and the optimisation design for high-performance turbomachinery in the near future.

Key words: flow–structure interactions

† Email address for correspondence: dxie@nwpu.edu.cn

1. Introduction

Aircraft engine blades, and their incorporation into a turbofan, turboprop or any other engine configuration, are critical components that have significant effects on the performance and safety of aviation. Concurrently, efforts are made to develop engines that meet the growing demand for enhanced performance while ensuring structural integrity and safety assurance, represented by a series of modern engine development plans proposed by the US military, including the Integrated High-Performance Turbine Engine Technology (IHPTET), Versatile Affordable Advanced Turbine Engines (VAATE) and Adaptive Versatile Engine Technology (ADVENT); see Ballal & Zelina (2004) and Hong & Collopy (2005). Thus, blade design prioritises characteristics such as lightweight construction, thin profiles and the capacity to withstand higher pressures, significantly increasing the potential for aeroelastic issues that lead to blade-off accidents. As exemplified by incidents such as the engine failure of British Midland Flight 92 in 1989, resulting in 47 fatalities, blade failures have occurred with concerning frequency in recent years, including the blade-related accidents that have been reported in cases involving Southwest Airlines Flight 1380 in 2018, Delta Air Lines Flight 1425 in 2019 and China Eastern Airlines Flight MU712 in 2023, indicating the necessity for comprehensive investigations and scholarly attention to the aeroelasticity of engine blades. The main phenomenon of aeroelastic instability is flutter, characterised by self-excited vibrations that pose an obstacle to the progress of advanced aircraft engines.

The complex flow around the blade produces a wide range of difficult-to-identify aerodynamic characteristics. Saunders & Marshall (2015) delved into vortex reconnection during vortex cutting by a blade, revealing complex phases and mechanics. Leclercq & De Langre (2018) investigated the reconfiguration of elastic blades in oscillatory flow and identified four kinematic regimes. Kingan & Parry (2020) addressed acoustic theory in contrarotating propellers, emphasising the effects of blade sweep on wake interaction noise. Lengani *et al.* (2022) focused on laminar–turbulent transition around low-pressure turbine blades using proper orthogonal decomposition (POD). Together, these investigations underscore the complexity and further emphasise the challenges associated with identifying properties in coupled aeroelastic problems.

Various investigations have highlighted the influence of shock waves on aeroelastic stability, with findings ranging from destabilising effects behind the shock to stabilising effects of the shock itself (Carstens & Belz 2001). Vahdati *et al.* (2001) came to the conclusion that the separation region behind the shock had a destabilising effect while the shock itself had a stabilising effect. Srivastava & Keith (2012) discovered that the location of the shock wave and the interblade phase angle (IBPA) of blade motion determined the shock wave's effect on blade stability. However, Aotsuka & Murooka (2014) demonstrated the stabilising effect of the separation area brought on by the interaction between the shock and boundary layer. In addition, the tip clearance flow, as demonstrated by researchers, significantly affects aeroelastic stability. Fu *et al.* (2015) showed the variation of aerodynamic damping is not monotonic, but a trend of first decrease and then increase with the rising of tip gap size, whereas Sun *et al.* (2019) found that the global aerodynamic damping for the least-stable IBPA increases with the tip gap height. Zheng *et al.* (2020) discovered the intensity of the tip vortex and shock wave are the key factors affecting the aeroelastic stability of the rotor when the tip gap size increases. These factors, alongside considerations such as blade mode and reduced velocity (Zhang, Wang & Xu 2013) and twist-induced pressure leading to destabilisation (Dong, Zhang & Lu 2023) contribute to the complexity of aeroelasticity analysis in this field. In summary, despite ongoing

research efforts, the intricate interplay of these factors in aeroelastic behaviour and flutter mechanisms presents a challenging and evolving area of study.

As determined by the National Transportation Safety Board (NTSB), the 2018 Southwest Airlines case illustrated premature fatigue cracks in CFM56 engines, resulting in blade failure (NTSB 2019). NASA has identified blade vibration-induced fatigue issues that contribute to 10–50% of engine-related accidents (Ramsey 2006). Therefore, it is imperative to address a critical structural issue: engines, despite having stability margins, are susceptible to failure caused by the development of fatigue cracks. Such damage within the structure plays a fundamental factor in blade flutter, with the flow field serving as a source of energy absorption for vibrations. Thus, the influence of structural damage on aeroelasticity represents a key consideration deserving further investigation. Kim, Vahdati & Imregun (2001) analysed aeroelastic stability for damaged blades with bird-strike impairments, noting stability reductions for moderate-to-severe damage. Muir & Friedmann (2016) investigated the aeroelastic response in fan stages with strike impact deformation. Mai & Ryu (2020) examined the effect of damage location on gas turbine performance, observing a thermal stress surge near damage sites. The majority of research on damaged blade aeroelasticity focuses on post-accident (e.g. bird-strike) performance, where the blade's geometry is altered. However, limited attention has been devoted to the aeroelastic instability process induced by internal structural fatigue damage.

The presence of such damage can be defined as changes in the dynamic system and will adversely affect the current or future performance of the system. Thus, research typically begins by focusing on two characteristics of material properties: structural stiffness and strength. Hassiotis (2000) simulated the damage with a known decrease in the stiffness of elements in the frame and developed an algorithm to detect and locate the magnitude and the location of such damage. Xie, Xu & Dai (2019) explored the effect of structural damage on the aeroelastic stability of supersonic plates, where structural damage is a local bending stiffness loss with various levels, extents and positions. Fayyadh & Raza (2022) investigated how different damage levels and scenarios affect dynamic-based and static-based stiffness indices representing stiffness deterioration for reinforced-concrete structures. Regarding strength, Zhang *et al.* (2021) summarised the strength loss correction formulae based on stiffness loss under different damage conditions of the hull girder. Gao *et al.* (2022) presented a pair of residual strength and residual stiffness models based on a unified fatigue damage formula, and predicted fatigue life under variable amplitude cyclic loading for composite laminates. Due to the primary focus on the aeroelasticity of damaged blades, the current research in this paper does not consider changes in strength. Instead, it concentrates on localised damage in specific areas (such as cracks or fatigue spots) that can reduce the stiffness of those particular regions. This approach ensures that the blade maintains its functional shape and performance characteristics.

Achieving these goals depends on precise and efficient numerical simulation to study flutter. Current blade flutter analysis technologies fall into three categories: classic uncoupled, fully integrated and partially integrated (Marshall & Imregun 1996). The classic method deals with this issue in an uncoupled manner, known as the energy method, via calculating the sum of work done by unsteady aerodynamic forces when the blade vibrates in a certain mode (Carta 1967). Researchers have developed energy methods by solving the Euler/Navier–Stokes (N–S) equations and achieved success (see Clark & Hall 2000; Sanders, Hassan & Rabe 2004; Vahdati, Simpson & Imregun 2011). An increase in the coupling influence among the blades within the airflow necessitates a more comprehensive analysis of the uncoupled approach (see Hall & Silkowski 1997; Namba & Nishino 2006; Kubo & Namba 2011). The fully integrated method

streamlines the aeroelastic problem-solving process by synchronising the integration of fluid and structural equations. Advances in rotor blade research have led to more precise analyses (see Yamamoto & August 1992; Forsching 1994; Vahdati, Sayma & Simpson 2005), yet a simulation requires extensive computational effort and faces convergence issues. The partially integrated method solves the fluid and structural equations through iterative data exchange, hereby optimising computational efficiency. Efforts (see Gnesin, Kolodyazhnaya & Rzadkowski 2004; Rzadkowski, Gnesin & Kolodyazhnaya 2010; Im & Zha 2014) have advanced in understanding the aeroelastic behaviour of turbines under various conditions. The partially integrated method strikes a balance between computational cost and accuracy, making it the preferred high-fidelity computational fluid dynamics (CFD)/computational structural dynamics (CSD) coupling method in this paper.

In summary, there are still several difficulties in analysing the aeroelastic behaviour and flutter mechanism/boundary. Commonly used public examples, such as Rotor37 and Rotor67, along with low-speed experimental benches designed by universities, typically do not exhibit flutter problems. The lack of flutter data may produce conflicting or even differing findings in studies on the main causes of flutter. Some studies only analysed aerodynamic damping decreases. Furthermore, real accidents highlight the need to investigate flutter under fatigue damage. Consequently, this paper first employs the partially integrated CFD/CSD coupling method, starting with static aerodynamic elastic deformation to construct a more accurate dynamic aeroelastic analysis. Subsequently, the damaged blade is modelled with local equivalent stiffness loss, and an investigation is conducted into the effect of damage parameters on aeroelastic stability. Finally, the SPOD method is employed to compare flow field characteristics under flutter and stable conditions, thereby helping to better understand the flutter mechanism of transonic damaged blades. The paper is organised as follows. In § 2, the methodology and process for subsystem modelling and coupling are introduced. Section 3 provides the numerical results and discussions, encompassing validation of models, and static and dynamic aeroelastic analysis conducted with a statically deformed blade aerodynamic configuration. In addition, the influence of damage parameters on the aeroelastic behaviour of rotating blades is explored and the flutter mechanisms under destabilising conditions are investigated via the SPOD method. Finally, § 4 provides the main conclusions of the present study.

2. Numerical methodologies

2.1. Geometry model

NASA Rotor67, a low-aspect-ratio transonic axial-flow fan rotor, is used to investigate the flutter mechanism of damaged blades in this work. Since the healthy Rotor67 never fluttered, it can serve as an ideal baseline for a steady aeroelastic system, facilitating the isolation and analysis of the effect of introduced damage without the confounding effects of previous flutter incidents. According to Strazisar *et al.* (1989), a comprehensive dataset is presented, encompassing flow conditions, blade coordinates, and experimental data. The fundamental design parameters are listed in table 1.

The flow field boundaries of the blades can be considered both periodic and symmetrical, owing to the rotational symmetry exhibited by the blade turbine. The flow characteristics observed on both sides of a single passage, exhibiting identical periodic relationships, can be regarded as forming the periodic boundary. Hence, the flow field of the whole ring cascade is simplified to a single passage, as depicted in figure 1. In addition, the lengths of the upstream and downstream meshes are extended and coarsened

Blade number	22
Tip clearance (mm)	1.016
Tip diameter at inlet (mm)	514
Tip diameter at outlet (mm)	485
Hub/tip radius ratio at inlet	0.375
Hub/tip radius ratio at outlet	0.478
Aspect ratio	1.56

Table 1. Basic design parameters of NASA Rotor67.

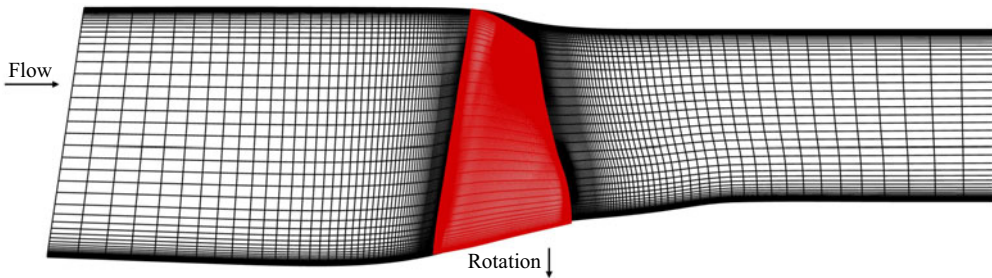


Figure 1. Single-passage mesh overview with an extend coarse inlet and outlet.

to eliminate the pressure wave reflection at the inlet and outlet boundaries (Dong *et al.* 2020). It is important to acknowledge that the blade model employed in this study does not address the influence of the hub/disc construction or its method of attachment. The model solely focuses on analysing the response of the blade structure itself. In addition, it is assumed that the grid on the hub remains stationary in the present investigation. Unless otherwise specified, the structural parameters of the blade in this study are taken as density $\rho = 4440 \text{ kg m}^{-3}$, Young's modulus $D = 142 \text{ GPa}$ and Poisson's ratio $\nu = 0.3$.

2.2. Subsystem model

2.2.1. Aerodynamic model

The three-dimensional Reynolds-averaged Navier–Stokes (RANS) equations in the rotating coordinate system attached to the rotating blade are employed in both steady and unsteady simulations. The rotational angular velocity vector is $\boldsymbol{\omega} = [\omega, 0, 0]^T$. The finite-volume method is used to discretise the foregoing governing equation,

$$\frac{\partial}{\partial t} \int_{\Omega} \mathbf{W} \, d\Omega + \oint_S \mathbf{F}_c \, dS + \oint_S \mathbf{F}_v \, dS = \int_{\Omega} \mathbf{Q} \, d\Omega, \quad (2.1)$$

where Ω represents the fixed control volume with boundary S , and the conservative variables \mathbf{W} , the convection flux \mathbf{F}_c , the viscous flux \mathbf{F}_v and the source term \mathbf{Q} can be

written in the following component forms:

$$\left. \begin{aligned} \mathbf{W} &= \begin{bmatrix} \rho \\ \rho u_i \\ \rho E \end{bmatrix}, \quad \mathbf{F}_c = \begin{bmatrix} \rho(u_i - \omega_j) \\ \rho u_i(u_i - \omega_j) + \rho \delta_{ij} \\ \rho E(u_j - \omega_j) + \rho u_j \end{bmatrix}, \quad \mathbf{F}_v = \begin{bmatrix} 0 \\ \sigma_{ij} \\ u_k \sigma_{ik} + \kappa \frac{\partial T}{\partial x_i} \end{bmatrix}, \\ \mathbf{Q} &= \begin{bmatrix} 0 \\ 0 \\ \omega \rho u_3 \\ -\omega \rho u_2 \\ 0 \end{bmatrix}, \end{aligned} \right\} (2.2a-d)$$

where ρ , p , E , K and T represent density, pressure, relative total energy per unit mass, thermal conductivity and temperature, respectively. In addition, r_i , u_i and ω_i refer to the displacement, velocity and velocity relative to the rotating frame of reference in three directions. We use σ_{ij} to represent the viscous stress tensor expressed with dynamic viscosity coefficient μ , which can be approximated by Sutherland’s law as a perfect gas:

$$\sigma_{ij} = \mu \left(\frac{\partial u_i}{\partial r_j} + \frac{\partial u_j}{\partial r_i} \right) - \frac{2}{3} \sigma_{ij} \mu \frac{\partial u_k}{\partial r_k}. \quad (2.3)$$

The discretised equations are temporally integrated using the second-order backward Euler technique, and spatial discretisation is achieved through the utilisation of the second-order upwind approach. All simulations are solved using double precision and the shear stress transport $k-\omega$ turbulence model. The stagnation parameter and flow angle are given at the inlet, whereas the radial pressure balancing condition is specified at the outflow. It is worth noting that a dependable determination of the stall point can be achieved by employing the outflow mass boundary condition.

2.2.2. Mechanical model

The structural dynamic response can be achieved by a finite-element analysis (FEA) across spatial variables and implementing temporal solutions with respect to the time variable of the global aeroelastic equations of motion:

$$\mathbf{M}\ddot{\mathbf{u}} + \mathbf{C}\dot{\mathbf{u}} + \mathbf{K}\mathbf{u} = \mathbf{F}_e, \quad (2.4)$$

where \mathbf{M} , \mathbf{C} and \mathbf{K} represent the system mass, damping and stiffness matrix, respectively, and \mathbf{F} is the external load vector of system nodes, which are obtained by integrating their respective unit matrices and vectors. We use $\ddot{\mathbf{u}}$, $\dot{\mathbf{u}}$ and \mathbf{u} to represent the acceleration, velocity and displacement of the structure, and \mathbf{C} , which includes both inherent structural damping and Coriolis force effects, has a limited effect and thus is mostly neglected for a greater safety design margin. Responses are computed at these discrete time points, initially utilising the central difference method, and subsequently refined and structured through the application of the Newmark Beta method.

As illustrated in figure 2, the damage under consideration is equivalent to a stiffness degradation by introducing a modified Young’s modulus, denoted as \bar{D} , in comparison with the healthy one D . Consequently, a stiffness degradation factor Sr is pronounced and defined with $Sr = \bar{D}/D$, serving as a quantitative measure of the damage level. It is important to note that a smaller Sr value corresponds to a lower stiffness and a

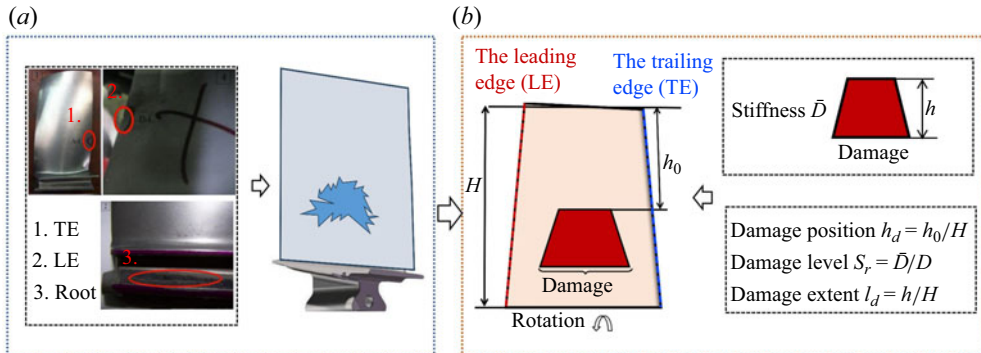


Figure 2. Schematic diagram of structural damage: (a) different fatigue failure positions of blades; (b) definition of damage parameters.

more severe level of damage. Moreover, it is essential to identify the potential damage location, which is denoted as h_0 , and the damage extent is defined by h . To provide a non-dimensional assessment of the damage, two parameters are introduced: h_d , expressed as the starting position of the damage along the blade height H , denoted as $h_d = h_0/H$; and l_d , which signifies the damage length relative to the blade height as $l_d = h/H$. These three parameters, namely S_r , h_d and l_d , collectively serve to define and quantify the damage level, position and extent within the blade.

What determines whether the time-domain iteration continues or not is the convergence of displacement in time history. The load on blades encompasses both the inertial force and aerodynamic force. The structural analysis commences by examining the displacement response of the structure following the application of minor disturbances. Notably, the damaged model solely accounts for the deterioration of local material properties, without altering the structural appearance. It is important to emphasise that the primary objective here is to investigate the effect and fundamental aeroelastic mechanisms of the blade and the effect of damage parameters, rather than delving into the intricacies of the damage processes.

2.3. Coupling model

The CFD and CSD are integrated into the time domain via their own independent classic solvers, as described in figure 3. The interface data between the fluid and solid domains are exchanged at each integrated time step. The flow solution is utilised to generate the unsteady aerodynamic load vector F_e , which is subsequently utilised as a boundary condition for the structural model in order to update the blade position. The aerodynamic mesh is afterwards adjusted to align with the structural motion by employing a grid interpolating technique. The iterative process culminates by computing the updated solution for unsteady flow at the new time step. This makes it possible to determine the unsteady pressures, which thus can be used as boundary conditions for the following time step.

The entire aeroelastic stability is determined through a two-part process, which is namely the analysis of static and dynamic aeroelasticity. The initial stage involves identifying the optimal aerodynamic configuration for the static aeroelastic analysis, referred to as the configuration during operational conditions while disregarding the thermal effect. Prior to initiating the dynamic aeroelastic computation cycle, a slight

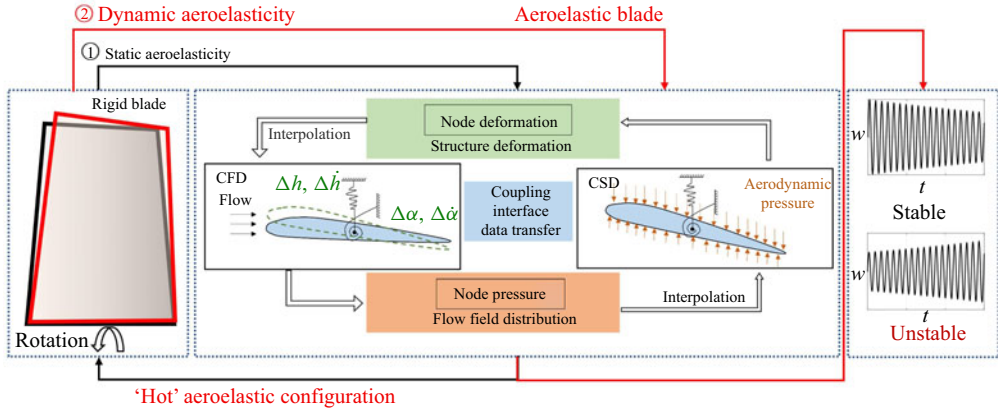


Figure 3. Schematic diagram of time-domain coupling solution.

perturbation deformation is executed on the static equilibrium shape. The investigation and evaluation of the blade flutter characteristics are conducted by analysing the displacement time history.

2.4. Spectral proper orthogonal decomposition method

The spectral proper orthogonal decomposition (SPOD) method (see Towne, Schmidt & Colonius 2018; Schmidt & Colonius 2020; Ji *et al.* 2023) achieves unsteady flow analysis by extracting the main components of flow field snapshots from time series data. The transition process from time to frequency domain is shown in figure 4, which consists of overlapping time-domain segmentation, discrete Fourier transform (DFT) and frequency domain reordering. Taking the unsteady pressure data of the flow field as input, the mode extraction starts from the construction of the snapshots matrix, which can be expressed in the form of column vector $\bar{Q} = [q_1, q_2, \dots, q_J]$. With Welch's method, the snapshot matrix is divided into multiple overlapping block matrices, and the n th block snapshot matrix can be defined as

$$\bar{Q}^{(n)} = [q_1^{(n)}, q_2^{(n)}, \dots, q_{N_f}^{(n)}], \quad n = 1, 2, \dots, N_b, \quad (2.5)$$

where N_b is the number of blocks and N_f is the number of snapshots in each block. Taking N_o as the number of snapshots overlapped between each block, the k th snapshot of the n th block is

$$q_k^{(n)} = q_{k+(n-1)(N_f-N_o)}, \quad k = 1, 2, \dots, N_f. \quad (2.6)$$

In the follow-up solution, $N_f = 2^n$, $n = 4, 5, \dots, 8$ and $N_o = N_f/2$, which change with snapshot data length with the need to guarantee $N_b > 20$. For each block, DFT is used to obtain the new snapshots matrix, which is recorded as

$$\hat{Q}^{(n)} = [\hat{q}_1^{(n)}, \hat{q}_2^{(n)}, \dots, \hat{q}_{N_f}^{(n)}], \quad n = 1, 2, \dots, N_b. \quad (2.7)$$

Flutter mechanism of a damaged transonic rotor blade

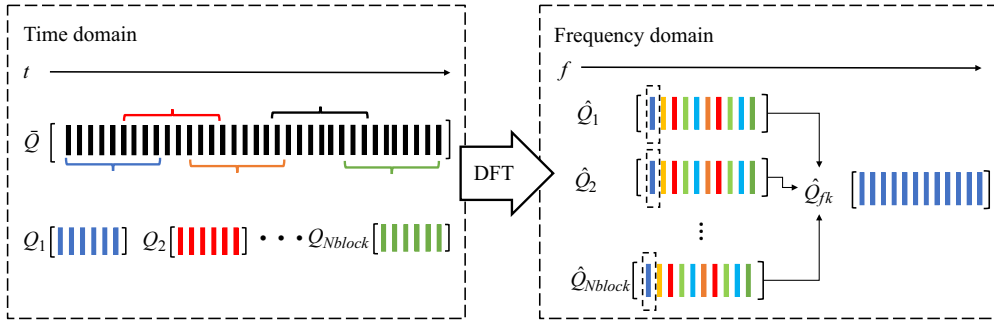


Figure 4. Illustration of SPOD method modal extraction (Ji *et al.* 2023).

The present snapshots of the blocks are

$$\hat{\mathbf{q}}_k^{(n)} = \frac{1}{\sqrt{N_f}} \sum_{j=1}^{N_f} w_j \mathbf{q}_j^{(n)} \exp(-i2\pi(k-1)) \left[\frac{(j-1)}{N_f} \right], \quad k = 1, \dots, N_f, n = 1, \dots, N_b, \quad (2.8)$$

$$w(j) = a_0 - (1 - a_0) \cos\left(\frac{2\pi j}{N_f - 1}\right), \quad 0 \leq j \leq N_f - 1. \quad (2.9)$$

The weight w_j is the value of the window function, which is used to reduce the spectrum leakage caused by the aperiodicity of each block. Here, $\hat{\mathbf{q}}_k^{(n)}$ is the Fourier transform at the frequency f_k in the n th block, the corresponding frequency f_k is

$$f_k = \begin{cases} \frac{k-1}{N_f \Delta t} & k \leq N_f/2, \\ \frac{k-1-N_f}{N_f \Delta t} & k > N_f/2. \end{cases} \quad (2.10)$$

The correlation matrix at f_k is

$$\mathbf{S}_{f_k} = \frac{\Delta t}{sN_b} \sum_{n=1}^{N_b} \hat{\mathbf{q}}_k^{(n)} \left(\hat{\mathbf{q}}_k^{(n)}\right)^H, \quad (2.11)$$

$$s = \sum_{j=1}^{N_f} w_j^2. \quad (2.12)$$

The Fourier components of each block are arranged in ascending order of frequency f_k , and a new snapshot matrix is introduced:

$$\hat{\mathbf{Q}}_{f_k} = \sqrt{\chi} \left[\hat{\mathbf{q}}_k^{(1)}, \hat{\mathbf{q}}_k^{(2)}, \dots, \hat{\mathbf{q}}_k^{(N_b)} \right], \quad (2.13)$$

where $\chi = \Delta t / (sN_b)$ with Δt as the sampling time step, and thus the correlation matrix at f_k is

$$\mathbf{S}_{f_k} = \hat{\mathbf{Q}}_{f_k} \left(\hat{\mathbf{Q}}_{f_k}\right)^H. \quad (2.14)$$

The spectral proper orthogonal decomposition modes (SPOMs) are obtained by solving the eigenvalue problem for each frequency-dependent matrix \mathbf{S}_{f_k} .

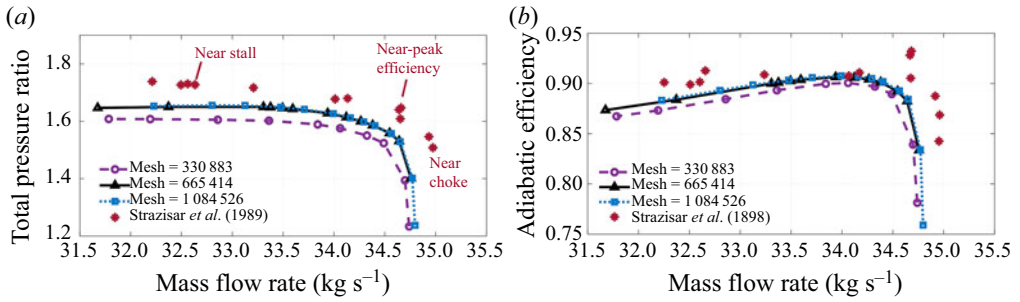


Figure 5. Mesh-dependence test based on a rigid blade: (a) total pressure ratio; (b) adiabatic efficiency.

3. Results and discussion

In order to examine the aerodynamic stability of NASA Rotor67, it is necessary to simulate the working line at the designated operational velocity of 16 043 rpm. Based on the current velocity, the Mach number at the blade tip is calculated to be 1.38. At the design condition, the flow rate is recorded as 33.15 kg s⁻¹, whereas the pressure ratio is measured to be 1.63. Furthermore, the flow rate at the choke point on the work line is 34.96 kg s⁻¹. A time-domain analysis is performed to investigate the effect of different operating circumstances on the working thread by altering the exit pressure. The temporal increment employed for the subsequent computation is experientially taken as $\Delta t = 1.25 \times 10^{-5}$ s, which denotes 1/200 of the reciprocal of the first-order natural frequency.

3.1. Validation of coupling model

Initially, a comprehensive examination of mesh dependency is undertaken, concurrently with an assessment of solver accuracy. This entails the utilisation of multiple meshes, which are subsequently juxtaposed against standard experimental conditions (Strazisar et al. 1989). The primary focus is on two pivotal parameters: the total pressure ratio P_{rc} and adiabatic efficiency η_c , as illustrated in figure 5:

$$P_{rc} = \frac{P_{t2}}{P_{t1}}, \quad \eta_c = \frac{1 - (P_{t2}/P_{t1})^{(\gamma-1)/\gamma}}{1 - T_{t2}/T_{t1}}. \quad (3.1a,b)$$

The prevailing approach utilised in the examination of aerodynamic performance involves the treatment of structures as rigid entities, facilitating the exploration of flow field characteristics around them through steady simulations. Consequently, the initial processing of the conventional static tip clearance of 1.016 mm has been executed. The outcomes demonstrate that the mesh comprising 665 414 cells attains a favourable balance between computational precision and cost. Nonetheless, a disparity is shown while contrasting the obtained results with the experimental data. The findings reveal that the rigid blades portray a decreased total pressure level near the stall point (figure 5a), a diminished choke mass flow rate and a forward shift of the near-peak efficiency point (figure 5b), which does not account for aeroelastic effects present in the actual experiments.

Figures 6 and 7 delineate the flow field characteristics observed on the typical surface, i.e. 10 % span from the shroud. These figures facilitate a comparative analysis between the computed results and empirical observations. An evident rise of Mach number distribution is observed at the leading edge (LE; figure 6b) for working status near the peak efficiency

Flutter mechanism of a damaged transonic rotor blade

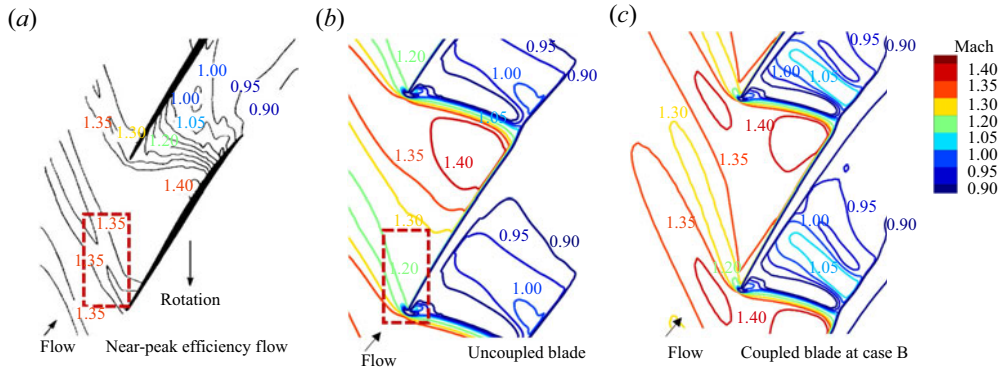


Figure 6. Contour plots of Mach number near the peak efficiency point (10 % span from the shroud): (a) experiment (Strazisar *et al.* 1989); (b) uncoupled blade; (c) coupled blade at Case B.

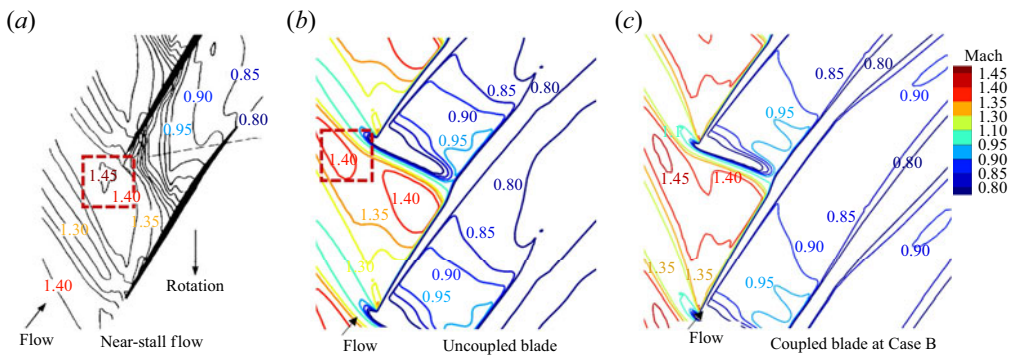


Figure 7. Contour plots of Mach number near the stall point (10 % span from the shroud): (a) Experiment (Strazisar *et al.* 1989); (b) uncoupled blade; (c) coupled blade at Case B.

Cases	Normalised mass flow rate	P_{rc}	η_c	Characteristics
A	0.996	1.532	0.882	Near choke
B	0.975	1.628	0.906	Near peak efficiency
C	0.923	1.654	0.902	Near stall

Table 2. Solution cases of static aeroelastic analysis.

point. Furthermore, complications are observed in the maximum Mach number between blades for the conditions near stall (figure 7b). These circumstances directly contribute to discrepancies in the placement of shock waves and the magnitude of aerodynamic pressure. As a result, the deformation of the elastic blade is ascertained through the application of static aeroelasticity, which hinges on the integration of CFD and CSD. In distinction from conventional methodologies, which often provide a one-step solution for force-induced deformations, the current approach employs the developed coupling model to advance the analysis in the time domain. Three operating conditions as specified in table 2 are chosen to represent typical performance for the static aeroelastic solution.

The deformation solution of the coupled blade is presented in figure 8. It is important to emphasise that the discrepancy between Cases B and C is negligible, suggesting a

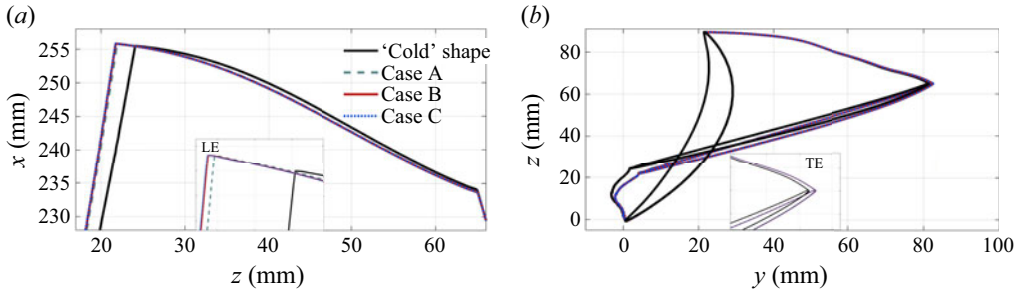


Figure 8. Solution of static aeroelastic configurations of Cases A, B and C: (a) z - x ; (b) y - z .

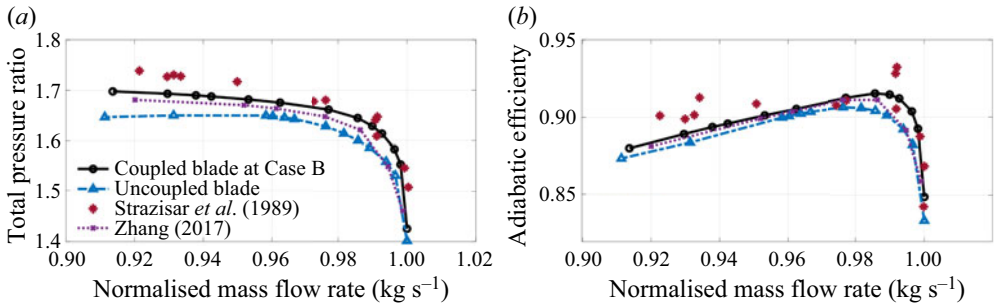


Figure 9. Aerodynamic performance comparison: (a) total pressure ratio; (b) adiabatic efficiency.

convergence in the findings. It is apparent that, apart from undergoing radial stretching, the local blade section also undergoes bending and untwisting. This phenomenon becomes increasingly pronounced as the radius increases and leads to a non-uniform distribution of tip clearance. Case B is thoughtfully selected as the instructive exemplar. Despite the relatively modest magnitude (with a maximum deformation of $\Delta(x, y, z) = (0.3302, 2.4984, -2.3240)$, mm), the incorporation of this coupled solution adeptly resolves the concerns associated with the flow field around rigid blades. Figure 6(c) elucidates the expanded range and heightened intensity of a larger transonic flow region at the LE, whereas figure 7(c) portrays an augmented maximum Mach number.

Furthermore, it is imperative to emphasise that numerous studies operate under the assumption that blades exhibit reduced and uniform tip clearances. Hence, the comparison with the simulation under the presumptions of 0.6-mm tip clearance (Zhang 2017) is depicted in figure 9. It becomes evident that the shape obtained through coupled simulation bears a closer resemblance to the experimental data, particularly in the proximity of peak efficiency. The present model has been validated and, thus, will subsequently serve as the foundation for the simulations in the following section.

3.2. Effect of ‘hot’ aerodynamic configuration

3.2.1. Static aeroelastic analysis

The variation in compressor performance can be attributed to the contrasting aerodynamic behaviours displayed by uncoupled and coupled blades. A fluid–structure coupling method has been applied to study the static aeroelastic problems of the ‘hot’ aerodynamic definition, where ‘hot’ means the updated blade shape undergoing design speed and temperature (Ramsey 2006), whereas the rigid blades are referred to as a ‘cold’ shape. It

Flutter mechanism of a damaged transonic rotor blade

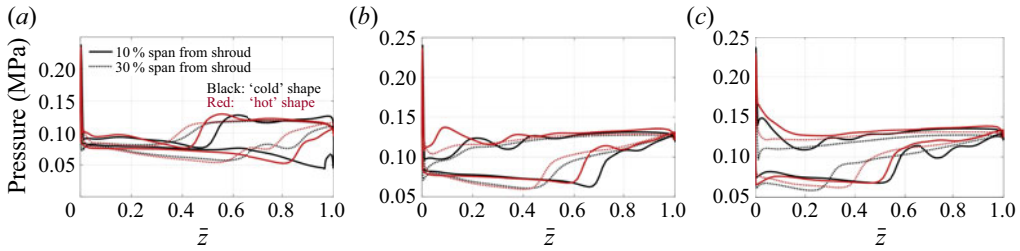


Figure 10. Surface pressure distribution of ‘cold’ and ‘hot’ shapes for: (a) Case A; (b) Case B; and (c) Case C.

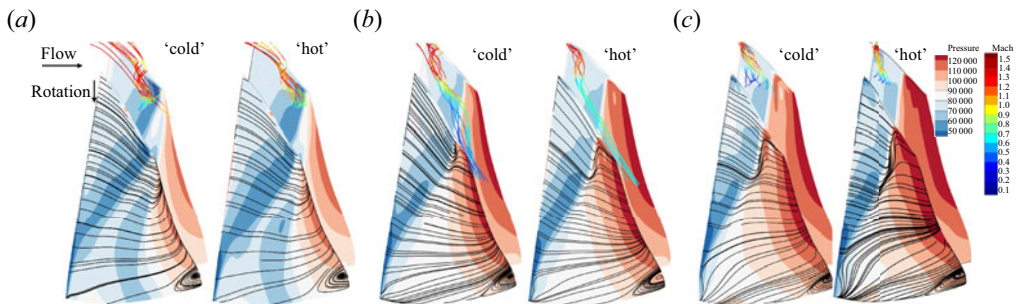


Figure 11. Contours of the pressure and surface streamline of ‘cold’ and ‘hot’ shapes for: (a) Case A; (b) Case B; and (c) Case C.

is crucial to recognise that even minor deformations possess the potential to influence the overall structural performance, as they can affect the flow field. Consequently, we delve deeper into analysing the deviations arising from the ‘hot’ aerodynamic configuration. [Figure 10](#) provides an illustration of the pressure distribution along chord-wise, whereas [figure 11](#) delineates the corresponding interblade streamline diagram.

Regarding Case B, an observable phenomenon is the heightened prominence of pressure distribution towards the LE in the ‘hot’ shape ([figure 10b](#)). Due to the slightly smaller clearance at the LE, fewer areas of tip vortex leakage are generated in the ‘hot’ shape from LE, allowing for a sustained flow velocity at the trailing edge (TE). In contrast, the tip vortex leakage in the ‘cold’ shape traverses the entire tip flow field until it reaches the TE of adjacent blades ([figure 11b](#)). Another distinction emerges in the distribution of shock waves along the blade surface. It is notable that the streamline on the ‘hot’ blade’s surface illustrates a forward shift of the separation zone, signifying a significant reduction in the pressure distribution along the suction surface. These differences gradually decrease as the position approaches the root.

The same phenomenon exists in Case C ([figures 10c](#) and [11c](#)). However, the larger difference appears at the 30% span compared with the 10% span from the shroud, which can be attributed to variations in the span-wise extent of the shock wave separation zone on the blade surface under different cases. In Case A, the pressure differential near the LE showcases a relatively subdued variation but a greater difference at the TE as shown in [figure 10\(a\)](#). This peculiarity is a consequence of the tip leaking vortex originating in closer proximity to the centre of the chord direction, as depicted in [figure 11\(a\)](#). The performance evaluation of a system based on a ‘cold’ shape can lead to inaccuracies due to the influence of ‘hot’ configurations. Since the operational point typically resides in the

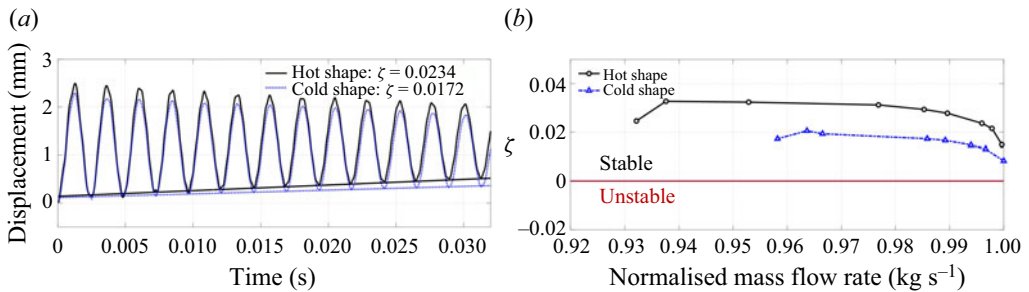


Figure 12. Dynamic aeroelastic response: (a) time history for ‘cold’ and ‘hot’ shape near stall; (b) damping coefficient of the working area.

vicinity of peak efficiency, Case B, representing the fixed ‘hot’ shape, was selected for subsequent exploration.

3.2.2. Dynamic aeroelastic analysis

Temporal aeroelastic characteristics of aeroelasticity are scrutinised to discern disparities and influential factors between the ‘cold’ and ‘hot’ conditions. Quantitative evaluation of aerodynamic stability under various operational scenarios entails the analysis of displacement convergence rates, serving as a crucial indicator of damping magnitude within an oscillating system. The exponential function $y = a + be^{-\zeta t}$ is employed to model the maximum value of the displacement response curve, with ζ signifying the damping coefficient. The dynamic aeroelastic solution commences by applying minor perturbations to the ‘hot’ shape derived from the static aerodynamic results. Subsequently, the analysis progresses into the time domain to capture time-varying phenomena.

The maximum deformation occurs at the LE of the blade tip. Figure 12 illustrates the time-domain motion for the near-stall operating state and provides results of aeroelastic stability verification within the operational range. Significantly, compared with the ‘hot’ shape, the ‘cold’ shape exhibits smaller vibration amplitudes and faster decay rates (figure 12a), primarily attributed to its lower pressure levels. However, the stall point resulting from vibration is notably advanced across the entire operational range when compared with the behaviour observed in the ‘hot’ shape. Moreover, although a sudden drop in aeroelastic stability near stall is observed in both cases, the ‘cold’ shape experiences an untimely increase before reaching this condition (figure 12b).

The distribution of displacement and equivalent stress at the extreme position of structural motion are depicted in figure 13, considering both the span-wise and chord-wise directions. Observing the deformation at the LE, it is notable that it experiences a rapid change with an increase in blade height. However, the change is less pronounced at lower positions but exhibits a significant increase after surpassing 40 % of the blade height at TE (figure 13a). When examining the equivalent strain energy and stress at the blade tip, where deformation is most significant, a stress concentration effect extending from the root to 70 % in the span-wise direction is observed (figure 13b,d). In terms of chord distribution, the stress level is notably higher at 30 % and 70 % than that at 10 % span from the shroud, with the peak value occurring between 1/3 and 2/3 from the LE (figure 13c).

Based on the simulation, it can be concluded that there is no danger of flutter before the stall threshold within the design speed for NASA Rotor67. Furthermore, the presence of vibration induces stress concentration inside the blade structure, extending from the root

Flutter mechanism of a damaged transonic rotor blade

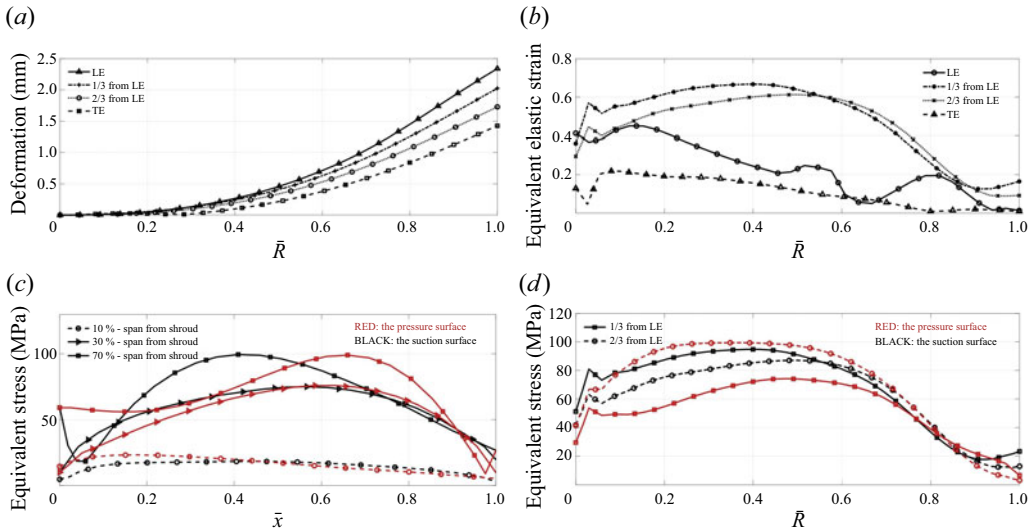


Figure 13. Structural load at the maximum point: (a) deformation at the LE, 1/3 from the LE, 2/3 from the LE and the TE; (b) equivalent elastic strain at the LE, 1/3 from the LE, 2/3 from the the LE and the TE; (c) equivalent stress at 10 %, 30 % and 70 % span from the shroud; (d) equivalent stress at 1/3 and 2/3 from the LE of the pressure surface and the suction surface.

to the middle section, as well as the central chord section. These phenomena elucidate the potential locations of fatigue-induced cracks.

3.3. Dynamic aeroelastic analysis of damaged blade

3.3.1. Effect of damage parameters

Representative damage parameters are selected for investigation based on the available results in figure 2. In the chord-wise distribution, the studied damage is limited to a distance of 1/3 to 2/3 of the LE span-wise damage starts at 30 %, 60 % and 80 % span from the shroud and ends at the root, i.e. $h_d = 0.3, 0.6$ and 0.8 . Take $h_d = 0.3$ as an example, damage extent l_d is determined by dividing the remaining 70 % blade height into three parts, i.e. $l_d = 0.3, 0.5$ and 0.7 . Similarly, $h_d = 0.6$ corresponds to $l_d = 0.2$ and 0.4 , whereas $h_d = 0.8$ corresponds to $l_d = 0.2$. Finally, the damage level increases sequentially as $Sr = 0.1-1$ with $\Delta Sr = 0.1$. Effects of damage level, extent and position on the aeroelastic behaviours and stability boundaries are discussed in detail. The near-stall working state is employed for simulation with a total pressure ratio of $P_{rc} = 1.688$ and a non-dimensional flow rate of 0.94. All figures are plots of a typical point at the LE of the blade tip.

Figures 14 and 15 present the schematic diagram of span-wise damage and the damping coefficient ζ of above-mentioned cases for variable Sr , h_d and l_d . In this study, $h_d = 0.3$, representing the minimum damage location studied, corresponds to a position closer to the blade tip. For $l_d = 0.3$, the results indicate that the blade remains stable across all tested scenarios. In contrast to initial predictions, damaged blades with higher damage levels (lower Sr) exhibit a larger ζ within $Sr = 0.2 \sim 1$ upon examination of the effect of Sr . For $l_d = 0.5$, ζ displays similar behaviour within the range of $Sr = 0.4-1$ but experiences a sharp reduction from $Sr = 0.4$ to 0.1. The turning point, marking the transition from increasing to decreasing damping, is identified as the critical Sr here. Upon

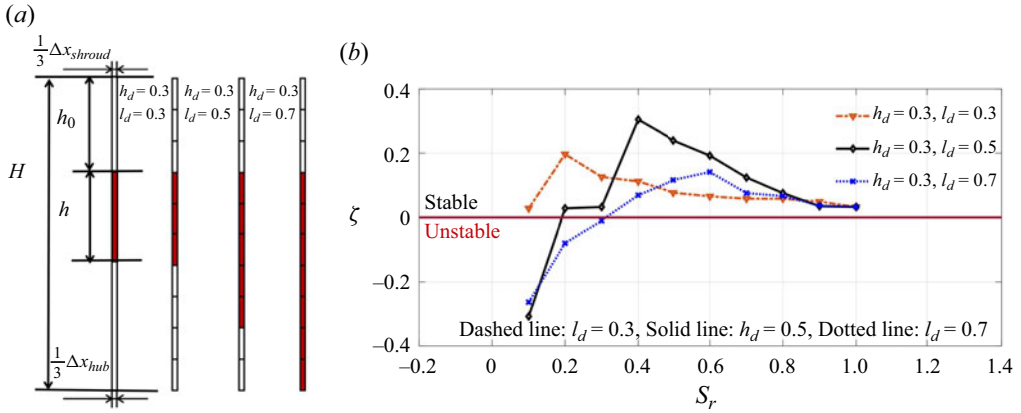


Figure 14. Damping coefficient ζ for varying $S = 0.1-1$, $l_d = 0.3, 0.5$ and 0.7 with $h_d = 0.3$ fixed.

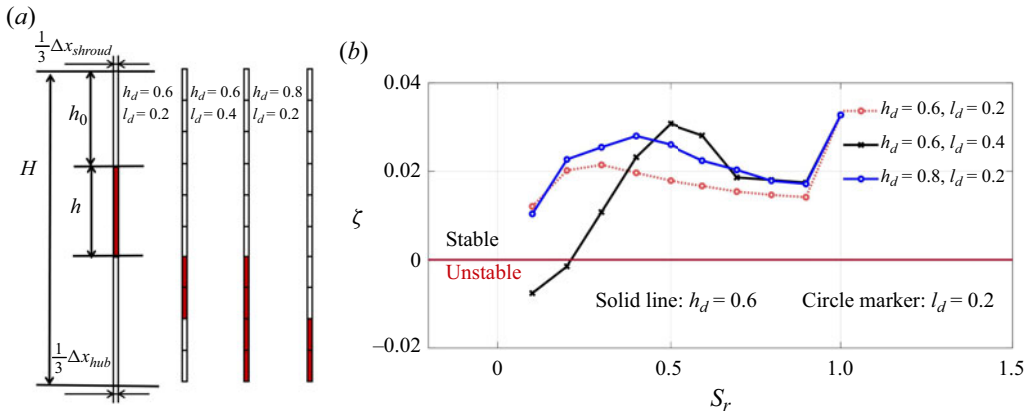


Figure 15. Damping coefficient ζ for varying $S = 0.1-1$, $l_d = 0.2$ and 0.4 with $h_d = 0.6$ fixed and $l_d = 0.2$ with $h_d = 0.8$.

further expansion to $l_d = 0.7$, the critical S_r increases to $S_r = 0.6$. In the above cases with $h_d = 0.3$, the damaged blade with $S_r = 0.2$, $l_d = 0.5$ and $S_r = 0.1 - 0.3$, $l_d = 0.7$ will experience aeroelastic instability. Under conditions of $h_d = 0.6$ and 0.8 , ζ of damaged blades are generally lower than those of healthy blades ($S_r = 1$), yet the aforementioned anomaly persists. In addition, as l_d increases, the critical S_r also gradually increases under the cases with $h_d = 0.3$ and 0.6 . Before the critical S_r threshold, the optimal ζ is observed under the condition of $h_d = 0.3$, $l_d = 0.5$. It is evident that before reaching the critical S_r threshold, damage regions that exhibit superior stability tend to experience a more significant decrease in stability after surpassing the critical S_r . Once the S_r threshold is surpassed, ζ undergoes a sharp decline, ultimately leading to the emergence of flutter.

To elucidate the effects of varying damage positions, a comparative analysis is conducted between the cases where $h_d = 0.6$, $l_d = 0.2$ and $h_d = 0.8$, $l_d = 0.2$. Specifically, the value of $h_d = 0.6$ signifies a location closer to the span-wise midpoint, whereas $h_d = 0.8$ indicates a position nearer to the root. The results show that damages occurring for $h_d = 0.6$ exhibit a more gradual change rate, lower damping levels and a smaller critical S_r before reaching the critical S_r . Thus, the combined effects of S_r , h_d and

Flutter mechanism of a damaged transonic rotor blade

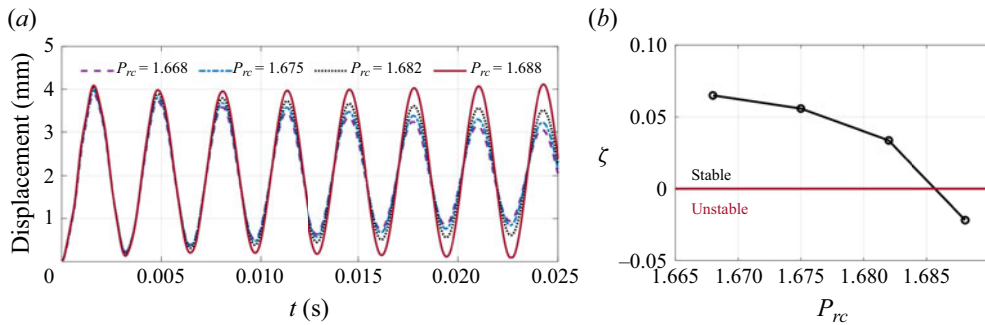


Figure 16. Dynamic aeroelastic for varying $P_{rc} = 1.668$ – 1.688 with $Sr = 0.2$, $h_d = 0.3$ and $l_d = 0.7$ fixed: (a) displacement in time history; (b) damping coefficient.

l_d reveal that damage occurring nearer the blade root poses a greater risk of instability, as evidenced by comparing the longitudinal distribution of the damaged blocks in the span-wise direction. Hence, the observed difference in the rate of change of the damaged blade's vibrational damping ζ with Sr can be primarily attributed to the combined effect of the location l_d and extent h_d of the damage incurred.

To sum up, the increase of damage level, as observed within a certain range can fortunately enhance aeroelastic stability. However, once it surpasses the critical Sr , the aeroelastic stability presents a rapid decrease or even results in instability. Moreover, the study demonstrates that the location and extent of damage mainly affect the aeroelastic stability by influencing the critical Sr value and the change rate of ζ with respect to Sr . Damage closer to the blade tip enhances stability, whereas damage nearer the blade root increases the risk of instability. This interesting finding could be utilised for weight optimisation of the rotor blade by adjusting an appropriate local material.

3.3.2. Exploration of blade flutter mechanism

In this section, the investigation into the distinctions between aeroelastic stability and instability conditions of damaged blades with $Sr = 0.2$, $l_d = 0.7$ and $h_d = 0.3$ will be conducted to explore the potential flutter mechanism for the blade. The response time history is depicted in figure 16 for varying total pressure ratios $P_{rc} = 1.668$, 1.675, 1.682 and 1.688. It is evident that with an increase in P_{rc} , aeroelastic stability decreases, with a relatively unchanged vibration frequency. Figure 17 illustrates the aerodynamic forces in the x (span-wise), y (circumferential-wise) and z (chord-wise) directions ($F_{x,y,z}$). Their amplitudes consistently vary with displacement magnitude, but much more notable differences are observed in the phase portraits of these forces. In the cases investigated, the phase of F_x exhibits a generally consistent pattern, with notable variations observed in its magnitude. When considering the variable F_y , a little phase advancement is seen as the value of P_{rc} increases. Significantly, the phase progression of F_z is particularly prominent. From the perspective of energy transfer, the phase discrepancies between unstable pressure and blade vibration result in variations in the work of the aerodynamic force on the blade, which have a negative effect on the aeroelastic stability at $P_{rc} = 1.688$.

To understand the mechanism behind the observed phase shift, a detailed examination on the flow field is necessary. The most significant phase change occurs in the z -direction, prompting us to focus on the flow field information at the blade's chord. Figures 18 and 19 present contour plots depicting the pressure and Mach number distributions in the flow field between the vibrating blades, respectively. At time $t = 0.0200$ s, the displacements

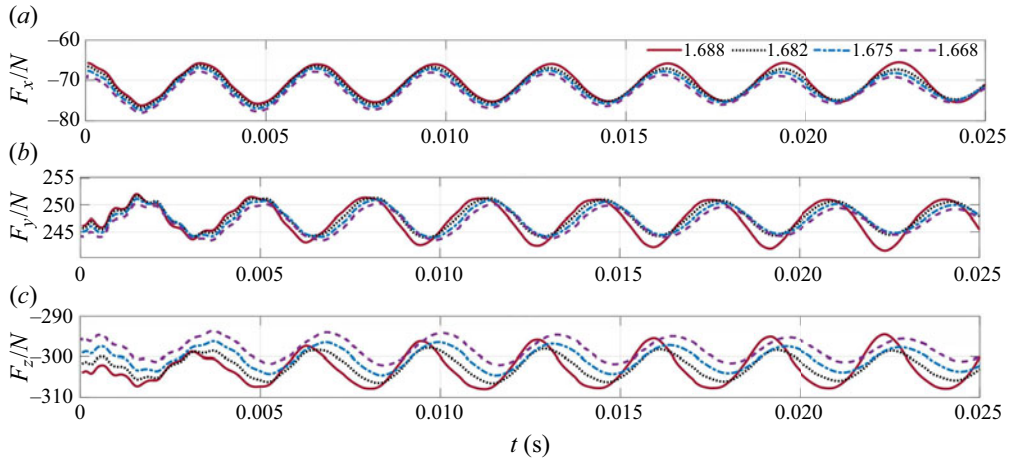


Figure 17. Aerodynamic force for varying $P_{rc} = 1.668\text{--}1.688$ with $Sr = 0.2$, $h_d = 0.3$ and $l_d = 0.7$ fixed.

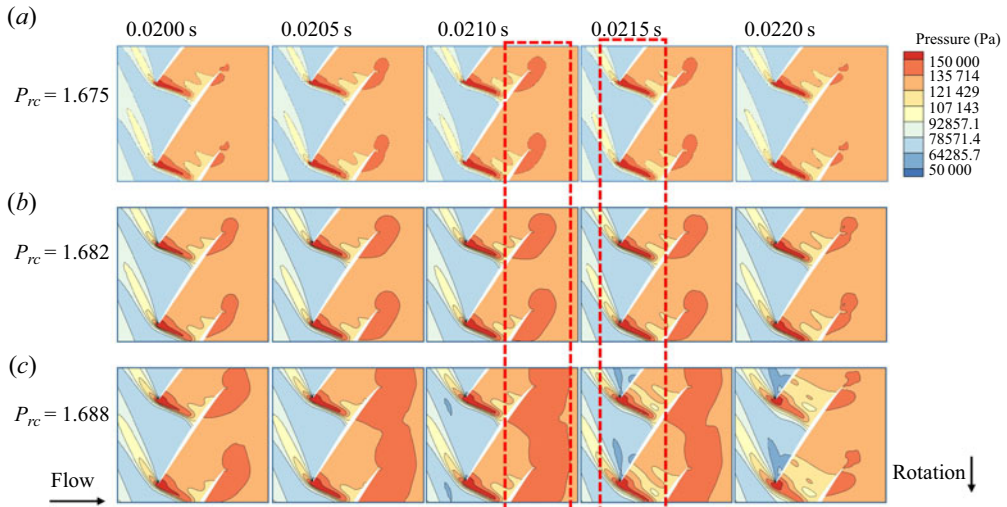


Figure 18. Pressure distribution at $t = 0.0200, 0.0205, 0.0210, 0.0215$ and 0.0220 s of 10% span from the shroud.

for the three conditions exhibit minimal differences. However, the flow field reveals substantial variations in the high-pressure region at the TE, which extends directly to the pressure surface of the neighbouring blade as displacement progresses, particularly notable at $t = 0.0205$ s, under $P_{rc} = 1.688$. This phenomenon leads to a heightened pressure difference between the blade's upper and lower surfaces, subsequently resulting in an increased displacement at $t = 0.0210$ s. In particular, distinctions in the flow field around the blades' LE become evident at this juncture, characterised by the appearance of a smaller low-pressure zone for the $P_{rc} = 1.688$ case, which is absent in the other two cases.

From $t = 0.0210$ to 0.0215 s, the low-pressure conditions near the LE exhibit a modest expansion, whereas there is a notable reduction in pressure conditions near the TE. By $t = 0.0220$ s, the three displacements had converged. However, significant changes in the

Flutter mechanism of a damaged transonic rotor blade

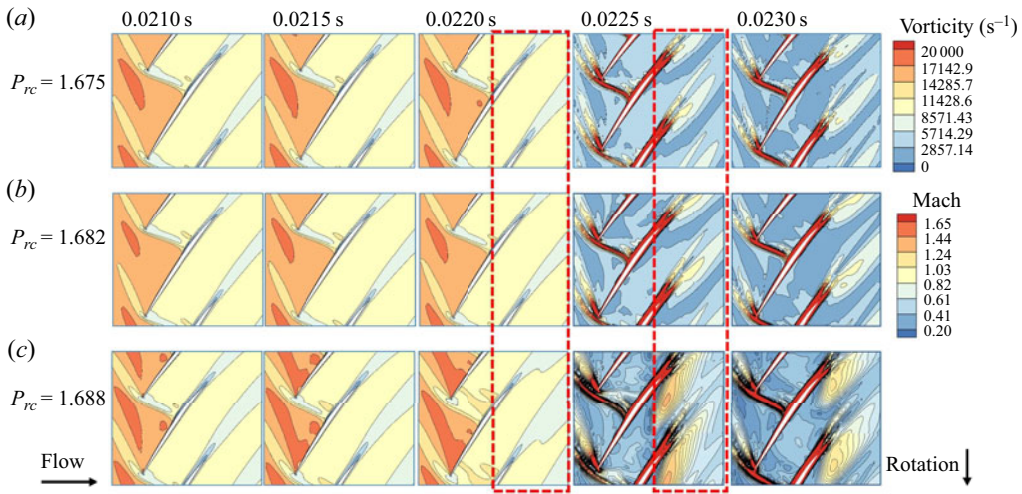


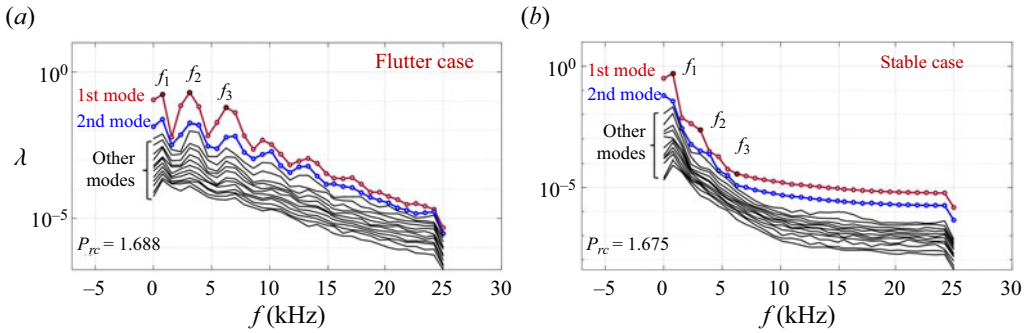
Figure 19. Mach number distribution at $t = 0.0200, 0.0205, 0.0210, 0.0215$ and 0.0220 s and vorticity distribution at $t = 0.0225$ and 0.0230 s of 10% span from the shroud.

TE low-pressure conditions for $P_{rc} = 1.668$ were detected, with a high-pressure regime in the blade's middle impacting nearby blades. These phenomena are reflected in the Mach number and vorticity distribution, as illustrated in figure 19, corresponding to a subsonic regime at the TE due to separation and a transonic regime at the LE. In the vorticity plots, it is evident that from $t = 0.0025$ to 0.0023 s, the higher-intensity shock wave at the LE under the $P_{rc} = 1.688$ condition significantly affects convergence. Simultaneously, towards the TE, there is a larger region of vortex detachment within the flow field between the blades, intensifying its impact on adjacent blades.

Upon observing the phenomena, it is noteworthy that the TE subsonic region (high-pressure region) stemming from boundary layer separation exhibits a dual functionality. Under stable conditions, this region serves to dampen vibrations. Conversely, during fluttering, as the high-pressure region expands onto adjacent blade surfaces, it paradoxically acts as a stimulus for vibrations, ultimately leading to instability. Thus, the distributions of the LE and TE lead to differences in the flow field divisions within the blade's midsection. Utilising vorticity plots to characterise this phenomenon can effectively elucidate the disparities between stability and instability. The aerodynamic instability condition at the LE is characterised by a more pronounced shock wave that converges towards the LE. Moreover, there are vortices with a wide range and high intensity located between the blades near the TE, contributing to instability and uneven energy distribution within the flow field. With the foregoing explanations, it is possible to conduct a preliminary analysis of the physical causes behind aeroelastic instability from two perspectives: aerodynamic work and flow field characteristics. The analysis serves to unveil the instability mechanisms and offers guidance for subsequent research.

3.3.3. SPOD modal identification of flutter mechanism

In a previous study (see Ji *et al.* 2023), some of the present authors clarified the ability of the SPOD method to extract global modes and their spectral advantages, which will not be further elaborated on here. Thus, as shown in § 3.3.2, the divergent and convergent cases at $P_{rc} = 1.688$ and $P_{rc} = 1.675$ are chosen to investigate the special characteristics via the SPOD method. A total of 500 snapshots of pressure distribution were collected in

Figure 20. SPOM energy spectrum: (a) $P_{rc} = 1.688$; (b) $P_{rc} = 1.675$.

the time domain of the three-dimensional flow field of the damaged blade with $Sr = 0.2$, $l_d = 0.7$ and $h_d = 0.3$. Each block contains 64 snapshot data, with adjacent block matrices overlapping by 50%.

The SPOD method decomposes the data into a set of orthogonal modes, each associated with a specific frequency and spatial structure. The resulting SPOD spectra (eigenvalues λ) are plotted vs (non-dimensional) frequency in figure 20. For each case, three frequencies are selected for characteristic SPOMs. Here f_1 – f_3 are 0.1328BPF (blade passing frequency) and its multiples. Both cases are dominated by the first-order mode, whereas higher frequencies and higher-order modes serve as complementary factors, enhancing and refining the effect. In terms of frequency, a small decrement in the energy levels associated with f_1 – f_3 is observed for the flutter case $P_{rc} = 1.688$. However, f_3 from stable case $P_{rc} = 1.675$ no longer serves as the primary distinguishing characteristic, because of its energy reduction of multiple orders of magnitude. To facilitate a comparative analysis, a representation of f_3 for $P_{rc} = 1.675$ is also included. Figures 21 and 23 show the first two SPOMs at f_1 – f_3 for $P_{rc} = 1.688$ and $P_{rc} = 1.675$ of 5% span from the shroud. The span-wise stream surface is determined by the periodic boundary between the blades, shown in figures 22 and 24. Due to the representative changes near the blade tip, the chord position is given by 5% span from the shroud.

In the span-wise direction of f_1 -1st for two cases, it is observed that the leakage vortex occurs at the tip gap near the LE of the blade (figures 22a and 24a), which interferes with the shock wave and generates disturbance chord-wise (figures 21a and 23a). Thus, the f_1 -2nd reveals the presence of small-scale disturbance clusters downstream of the shockwave chord-wise (figures 21d and 23d). However, these disturbance clusters dissipate rapidly within the flow passage as they propagate downstream. Moreover, f_1 -2nd for the flutter case $P_{rc} = 1.688$ indicates that the extent of the tip leakage flow results in a more extensive influence on the blade tip region. For f_2 -1st (figures 21b and 23b), the SPOMs show that the interaction between the tip clearance leakage vortices and the mainstream flow results in the formation of large-scale disturbance. Such disturbance propagates downstream along the chord-wise direction from the LE and concurrently spreads from the tip to the root of the blade (figures 22b and 24b). These occurrences in both flutter and stable cases suggest a potential correlation with the unsteady periodic fluctuations in the blade flow field.

Different modes appear in f_2 -2nd and f_3 . For the stable case, f_2 -2nd (figure 23e) has a phase difference in disturbance clusters compared with f_1 -1st. However, f_2 -2nd becomes even more intricate for flutter (figures 21e and 22e). This complexity is evident in the

Flutter mechanism of a damaged transonic rotor blade

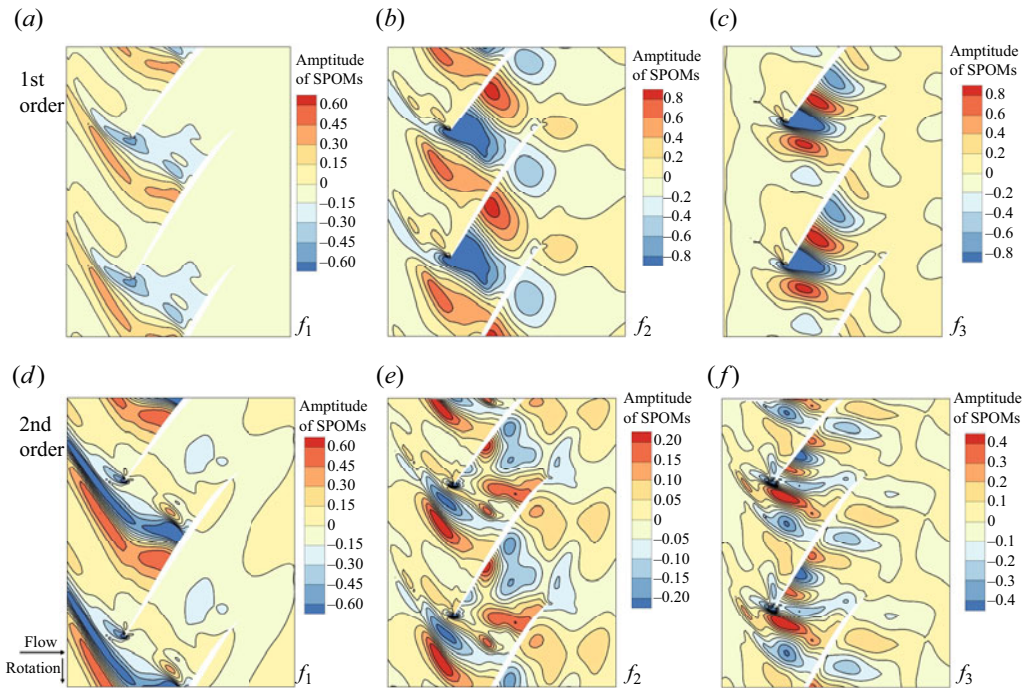


Figure 21. The first- and second-order SPOMs of 5% span from the shroud at $P_{rc} = 1.688$: (a) first order at f_1 ; (b) first order at f_2 ; (c) first order at f_3 ; (d) second order at f_1 ; (e) second order at f_2 ; (f) second order at f_3 .

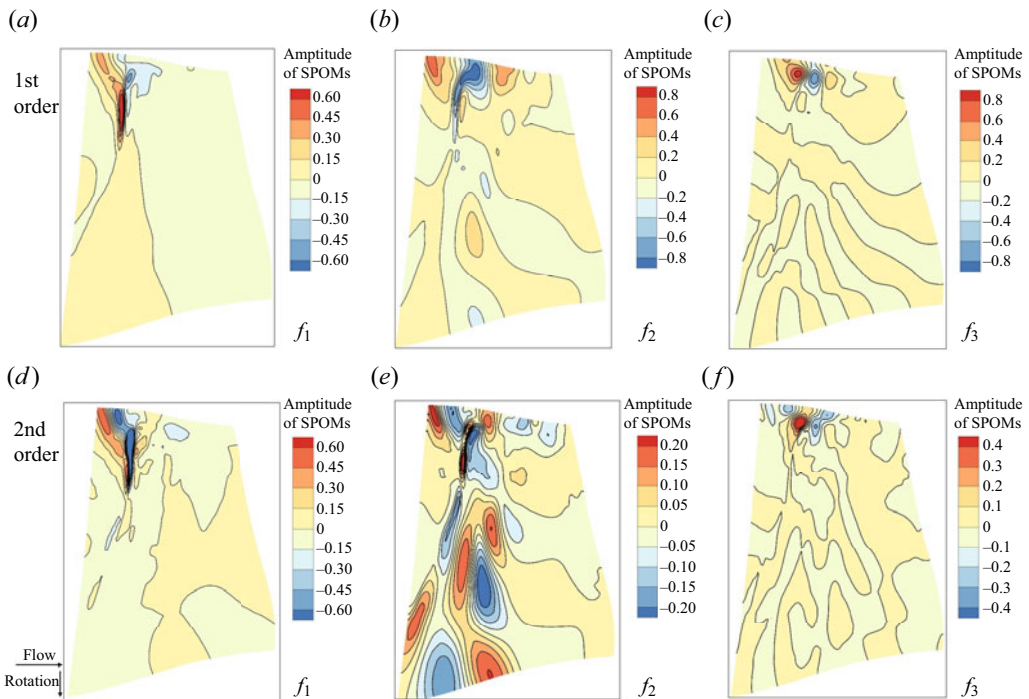


Figure 22. The first- and second-order SPOMs of span-wise stream surface at $P_{rc} = 1.688$: (a) first order at f_1 ; (b) first order at f_2 ; (c) first order at f_3 ; (d) second order at f_1 ; (e) second order at f_2 ; (f) second order at f_3 .

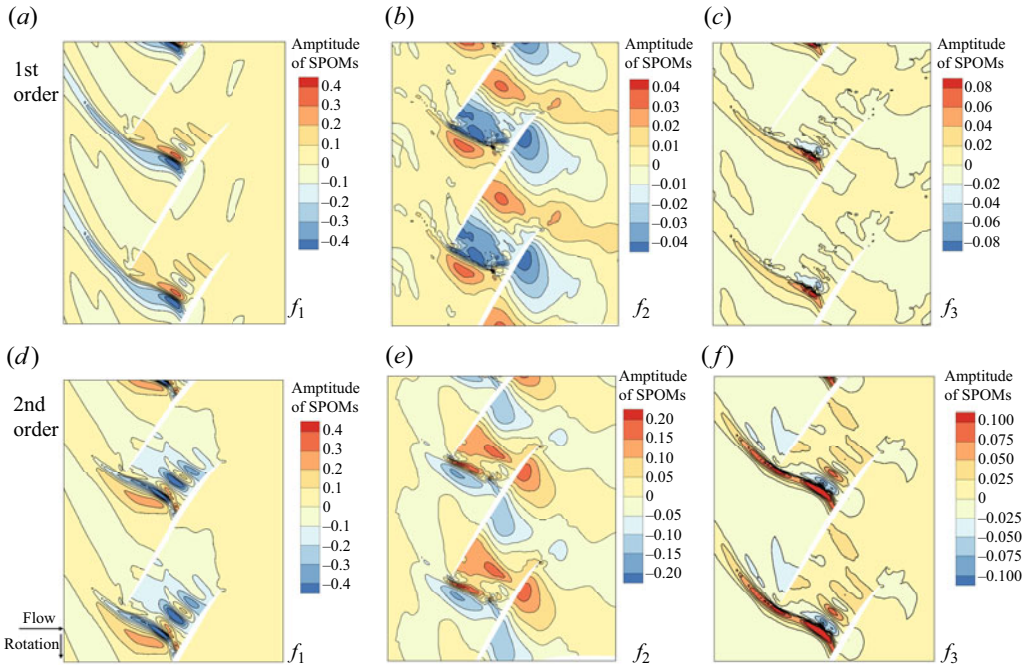


Figure 23. The first- and second-order SPOMs of 5% span from the shroud at $P_{rc} = 1.675$: (a) first order at f_1 ; (b) first order at f_2 ; (c) first order at f_3 ; (d) second order at f_1 ; (e) second order at f_2 ; (f) second order at f_3 .

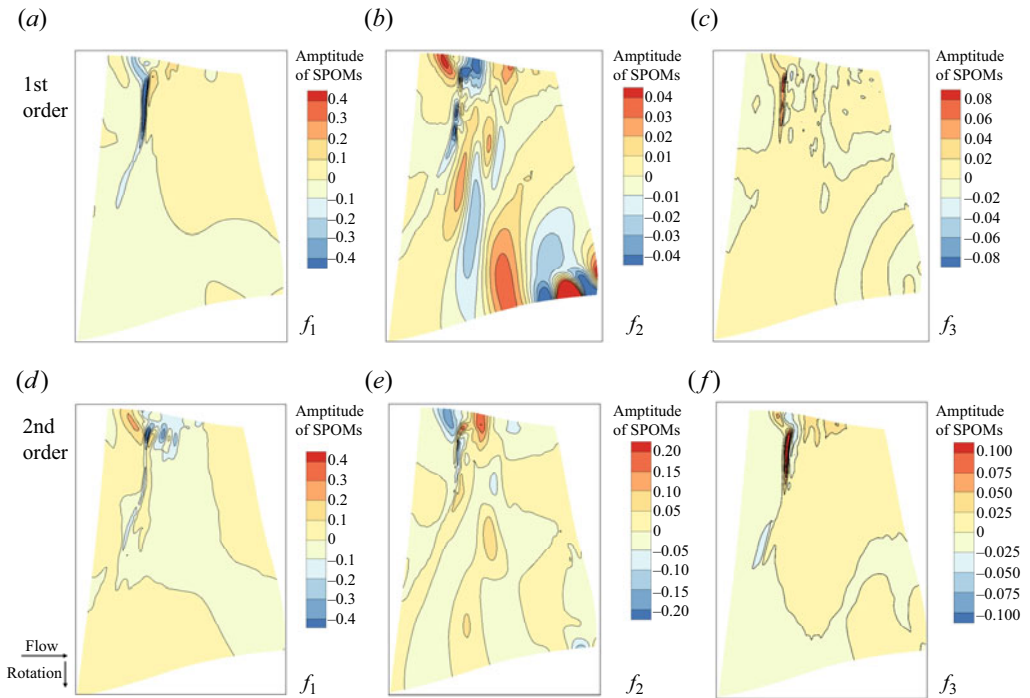


Figure 24. The first- and second-order SPOMs of span-wise stream surface at $P_{rc} = 1.675$: (a) first order at f_1 ; (b) first order at f_2 ; (c) first order at f_3 ; (d) second order at f_1 ; (e) second order at f_2 ; (f) second order at f_3 .

increased quantity of disturbance clusters. Despite being smaller scale compared with f_2 -1st, these disturbances maintain their intensity along both chord-wise and span-wise flow channels and engage in interactions among the blades. As expected, the f_3 for $P_{rc} = 1.675$ (figures 23c,f and 24c,f) exhibits a flow field structure similar to that of f_1 due to its lower energy. The phenomenon distribution of f_3 (figure 21c,f) resembles that of f_2 for $P_{rc} = 1.688$, yet the influence scope of the f_3 disturbance exhibits a backwards shift. These disturbance groups exist through the entire interblade channel in the chord direction, but no longer maintain their strength in the span-wise direction.

Overall, the SPOMs observed between the flutter and stable cases can be primarily summarised into two crucial factors. First, the high-frequency perturbation with a larger scale exhibits a distinct frequency characteristic that is intrinsic to the SPOD method. Second, the high-order small-scale perturbation clusters, which propagate across the flow channels, maintain their strength over a broader area, thus exerting a more widespread influence between blades.

4. Conclusions

This study was mainly conducted to predict the flutter boundary of transonic rotor blades such as the representative NASA Rotor67 with possible structural damage, which is parameterised with varying damage levels, extents and locations. Furthermore, the physical mechanism of rotor blade flutter has been explored in time and frequency domains. Specifically, a high-fidelity CFD/CSD coupling model in the time domain has been established for both static and dynamic aeroelastic analysis at a predetermined rotational speed (16 043 rpm), and SPOMs in the frequency domain have been identified for the evaluation of factors inducing fluttering instability, respectively.

The main conclusions are as follows.

- (i) The ‘hot’ configuration results in more accurate steady-state and aeroelastic results compared with the ‘cold’ shape. The differences are ascribed to variations in the flow field vortices, which are induced by the variable clearance between the blade tips.
- (ii) Curves of damping coefficient with damage level indicate that there is a critical threshold, below which aeroelastic stability is improved positively with increased damage level (Sr decreases accordingly), but inversely, a significant loss of stability is induced. The damage extent changes the critical Sr value and the damage location affects the change rate of the curve in terms of the damping coefficient with respect to Sr . In particular, damage located near the blade tip can enhance the aeroelastic stability, whereas the damage near the blade root will more likely induce instability.
- (iii) The numerical results on flutter analysis revealed that the boundary layer separation played inverse roles in stable and flutter conditions. In stable conditions, the high-pressure subsonic region induced from boundary layer separation provides damping and prevents vibrations from spreading. However, during flutter, the high-pressure region diffuses to adjacent blade surfaces, stimulating vibrations and finally triggering instability.
- (iv) The exploration of the flutter mechanism via the SPOMs reveals that the involvement of high-frequency large-scale disturbances are the key factor inducing flutter, and the high-order small-scale disturbances with slow dissipation further stimulate this phenomenon. These disturbances maintain their intensity and interact with each other, persistently causing extensive influence both chord-wise and span-wise.

In summary, by investigating the hot configuration, aeroelastically damaged blade and the flutter mechanism, this study has provided important insights into the aeroelastic behaviour of a transonic rotor blade. These results offer valuable information that can be used to guide the design of blade structures to reduce flutter risk and forecast rotor blade damage.

Acknowledgements. The authors gratefully acknowledge the technical support provided by the Multidisciplinary Flight Dynamics and Control Laboratory of the School of Astronautics, Northwestern Polytechnical University. The authors would also like to thank the Aeroelasticity Research Group of the Department of Mechanical Engineering and Materials Science, School of Engineering, Duke University for invaluable suggestions, insightful discussions and mentorship throughout this study.

Funding. This study was supported by the NSFC International (Regional) Cooperation and Exchanges Program (12211540709) and the National Natural Science Foundation of China (11972294).

Declaration of interests. The authors report no conflict of interest.

Author ORCIDs.

-  Chunxiu Ji <https://orcid.org/0000-0003-1079-4142>;
-  Zijun Yi <https://orcid.org/0009-0006-3915-6848>;
-  Dan Xie <https://orcid.org/0000-0002-9523-391X>;
-  Earl H. Dowell <https://orcid.org/0000-0001-6687-2467>.

REFERENCES

- AOTSUKA, M. & MUROOKA, T. 2014 Numerical analysis of fan transonic stall flutter. In *Proceedings of the ASME Turbo Expo 2014*, vol. 7B, p. V07BT35A020. ASME.
- BALLAL, D.R. & ZELINA, J. 2004 Progress in aeroengine technology (1939–2003). *J. Aircraft* **41**, 43–50.
- CARSTENS, V. & BELZ, J. 2001 Numerical investigation of nonlinear fluid-structure interaction in vibrating compressor blades. *Trans. ASME J. Turbomach.* **123**, 402–408.
- CARTA, F.O. 1967 Coupled blade-disk-shroud flutter instabilities in turbojet engine rotors. *J. Engng Power* **89**, 419–426.
- CLARK, W.S. & HALL, K.C. 2000 A time-linearized Navier–Stokes analysis of stall flutter. *Trans. ASME J. Turbomach.* **122**, 467–476.
- DONG, X., ZHANG, Y. & LU, X. 2023 Fan flutter mechanisms related to blade mode shape and acoustic properties. *Trans. ASME J. Turbomach.* **145**, 091013.
- DONG, X., ZHANG, Y.F., ZHANG, Y.J., ZHANG, Z. & LU, X. 2020 Numerical simulations of flutter mechanism for high-speed wide-chord transonic fan. *Aerosp. Sci. Technol.* **105**, 106009.
- FAYYADH, M.M. & RAZA, H.A. 2022 Experimental assessment of dynamic and static based stiffness indices for RC structures. *Structures* **45**, 459–474.
- FORSCHING, H. 1994 Aeroelastic stability of cascades in turbomachinery. *Prog. Aerosp. Sci.* **30**, 213–266.
- FU, Z., WANG, Y., JIANG, X. & WEI, D. 2015 Tip clearance effects on aero-elastic stability of axial compressor blades. *Trans. ASME J. Engng Gas Turbines Power* **137**, 012501.
- GAO, J.X., ZHU, P.N., YUAN, Y.P., WU, Z.F. & XU, R.X. 2022 Strength and stiffness degradation modeling and fatigue life prediction of composite materials based on a unified fatigue damage model. *Engng Fail. Anal.* **137**, 106290.
- GNESIN, V.I., KOLODYAZHNAYA, L.V. & RZADKOWSKI, R. 2004 A numerical modelling of stator–rotor interaction in a turbine stage with oscillating blades. *J. Fluids Struct.* **19**, 1141–1153.
- HALL, K.L. & SILKOWSKI, P.D. 1997 The influence of neighboring blade rows on the unsteady aerodynamic response of cascades. *Trans. ASME J. Turbomach.* **119**, 85–93.
- HASSIOTIS, S. 2000 Identification of damage using natural frequencies and Markov parameters. *Comput. Struct.* **74**, 365–373.
- HONG, W.S. & COLLOPY, P.D. 2005 Technology for jet engines: case study in science and technology development. *J. Propul. Power* **21**, 769–777.
- IM, H. & ZHA, G. 2014 Investigation of flow instability mechanism causing compressor rotor-blade nonsynchronous vibration. *AIAA J.* **52**, 2019–2031.
- Ji, C.X., XIE, D., ZHANG, S.H. & MAQSOOD, A. 2023 Spectral proper orthogonal decomposition reduced-order model for analysis of aerothermoelasticity. *AIAA J.* **61**, 793–807.

Flutter mechanism of a damaged transonic rotor blade

- KIM, M., VAHDATI, M. & IMREGUN, M. 2001 Aeroelastic stability analysis of a bird-damaged aeroengine fan assembly. *Aerosp. Sci. Technol.* **5**, 469–482.
- KINGAN, M.J. & PARRY, A.B. 2020 Acoustic theory of the many-bladed contra-rotating propeller: the effects of sweep on noise enhancement and reduction. *J. Sound Vibr.* **468**, 115089.
- KUBO, A. & NAMBA, M. 2011 Analysis of interrow coupling flutter of multistage blade row. *AIAA J.* **49**, 2357–2366.
- LECLERCQ, T. & DE LANGRE, E. 2018 Reconfiguration of elastic blades in oscillatory flow. *J. Fluid Mech.* **838**, 606–630.
- LENGANI, D., SIMONI, D., PRALITS, J.O., DUROVIC, K., DE VINCENZI, L., HENNINGSON, D.S. & HANIFI, A. 2022 On the receptivity of low-pressure turbine blades to external disturbances. *J. Fluid Mech.* **937**, A36.
- MAI, T.D. & RYU, J. 2020 Effects of leading-edge modification in damaged rotor blades on aerodynamic characteristics of high-pressure gas turbine. *Mathematics* **8**, 2191.
- MARSHALL, J.G. & IMREGUN, M. 1996 A review of aeroelasticity methods with emphasis on turbomachinery applications. *J. Fluids Struct.* **10**, 237–267.
- MUIR, E.R. & FRIEDMANN, P.P. 2016 Forced and aeroelastic responses of bird-damaged fan blades: a comparison and its implications. *J. Aircraft* **53**, 561–577.
- NAMBA, M. & NISHINO, R. 2006 Flutter analysis of contra-rotating blade rows. *AIAA J.* **44**, 2612–2620.
- NTSB 2019 Left engine failure and subsequent depressurization, Southwest Airlines Flight 1380, Boeing 737-7H4, N772SW, Philadelphia, Pennsylvania, April 17, 2018, NTSB/AAR-19/03.
- RAMSEY, J.K. 2006 NASA Aeroelasticity Handbook, Volume 2: Design Guides, Part 2. *NASA Tech. Rep.* NASA/TP2006-212490/VOL2/PART2. NASA Glenn Research Center.
- RZADKOWSKI, R., GNESIN, V. & KOLODYAZHNAYA, L. 2010 Numerical modelling of fluid-structure interaction in a turbine stage for 3D viscous flow in nominal and off-design regimes. In *Proceeding of the ASME Turbo Expo 2010*, vol. 6, pp. 1299–1307. ASME.
- SANDERS, A.J., HASSAN, K.K. & RABE, D.C. 2004 Experimental and numerical study of stall flutter in a transonic low-aspect ratio fan blisk. *Trans. ASME J. Turbomach.* **126**, 166–174.
- SAUNDERS, D.C. & MARSHALL, J.S. 2015 Vorticity reconnection during vortex cutting by a blade. *J. Fluid Mech.* **782**, 37–62.
- SCHMIDT, O.T. & COLONIUS, T. 2020 Guide to spectral proper orthogonal decomposition. *AIAA J.* **58**, 1023–1033.
- SRIVASTAVA, R. & KEITH, T.G. JR. 2012 Influence of shock wave on turbomachinery blade row flutter. *J. Propul. Power* **21**, 167–174.
- STRAZISAR, A.J., WOOD, J.R., HATHAWAY, M.D. & SUDER, K.L. 1989 Laser anemometer measurements in a transonic axial-flow fan rotor. *NASA Tech. Paper* 2879.
- SUN, T., HOU, A., ZHANG, M. & PETRIE-REPAR, P. 2019 Influence of the tip clearance on the aeroelastic characteristics of a last stage steam turbine. *Appl. Sci.-Basel* **9**, 1213.
- TOWNE, A., SCHMIDT, O.T. & COLONIUS, T. 2018 Spectral proper orthogonal decomposition and its relationship to dynamic mode decomposition and resolvent analysis. *J. Fluid Mech.* **847**, 821–867.
- VAHDATI, M., SAYMA, A.I., MARSHALL, J.G. & IMREGUN, M. 2001 Mechanisms and prediction methods for fan blade stall flutter. *J. Propul. Power* **17**, 1100–1108.
- VAHDATI, M., SAYMA, A.I. & SIMPSON, G. 2005 Multibladerow forced response modeling in axial-flow core compressors. *Trans. ASME J. Turbomach.* **129**, 412–420.
- VAHDATI, M., SIMPSON, G. & IMREGUN, M. 2011 Mechanisms for wide-chord fan blade flutter. *Trans. ASME J. Turbomach.* **133**, 041029.
- XIE, D., XU, M. & DAI, H. 2019 Effects of damage parametric changes on the aeroelastic behaviors of a damaged panel. *Nonlinear Dyn.* **97**, 1035–1050.
- YAMAMOTO, O. & AUGUST, R. 1992 Structural and aerodynamic analysis of a large-scale advanced propeller blade. *J. Propul. Power* **8**, 367–373.
- ZHANG, X. 2017 Research on frequency domain nonlinear analysis method and its application for blade aeroelastic stability in turbomachines Northwestern Polytechnical University. PhD thesis, School of Engine and Energy.
- ZHANG, X., WANG, Y. & XU, K. 2013 Mechanisms and key parameters for compressor blade stall flutter. *Trans. ASME J. Turbomach.* **135**, 024501.
- ZHANG, Y., GUO, J., XU, J., LI, S. & YANG, J.J. 2021 Study on the unequivalence between stiffness loss and strength loss of damaged hull girder. *Ocean Engng* **229**, 108986.
- ZHENG, Y., GAO, Q., YANG, H. & XU, K. 2020 Aeroelastic vibration analysis of a 1.5 stage compressor. *Propuls. Power Res.* **9**, 26–36.